Journal of Applied Physics ARTICLE scitation.org/journal/jap

Nitrogen diffusion in zinc oxide

Cite as: J. Appl. Phys. **130**, 245702 (2021); doi: 10.1063/5.0070510
Submitted: 16 September 2021 · Accepted: 2 December 2021 ·
Published Online: 27 December 2021

N. H. Nickel[a] and M. A. Gluba[b]

AFFILIATIONS

Helmholtz-Zentrum Berlin für Materialien und Energie GmbH, Institut für Silizium-Photovoltaik, Kekuléstr. 5, 12489 Berlin, Germany

[a]**Author to whom correspondence should be addressed:** nickel@helmholtz-berlin.de
[b]**Present address:** Multirotor, Forstweg 1, 14656 Brieselang, Germany.

ABSTRACT

Nitrogen migration in ZnO was investigated by nitrogen isotope diffusion. The samples were deposited using plasma-assisted pulsed laser deposition. Nitrogen concentration depth profiles were obtained from secondary-ion-mass spectrometry measurements, and in gas effusion measurements, the molecular nitrogen flux was measured as a function of the heating rate. Measurements performed on sample stacks that were doped with isotopically enriched ^{15}N and ^{14}N in the top and bottom half of the samples, respectively, clearly demonstrate that nitrogen diffusion is governed by atomic diffusion and molecules are formed primarily at the sample surface. At high nitrogen concentrations, the diffusion coefficient, D, is thermally activated, while for low concentration diffusion, D is independent of temperature. The data can be described by a model, where N diffusion occurs between minimum energy positions by surmounting the barrier between sites at a saddle point. Separated in energy from the transport sites are deep levels with a concentration of $\approx 10^{18}$ cm^{-3}. For high-concentration diffusion, the N chemical potential, μ_N, resides at ≈1.36 eV below the migration saddle point. For low concentration diffusion, μ_N shifts deeper in energy with a rate of ≈2.8 meV/K as the temperature increases. From N effusion data, the nitrogen density-of-states is derived. For high N concentration diffusion, two peaks are observed at $E_S - \mu_N = -0.93$ and -1.26 eV, while for low N concentration diffusion, a prominent peak at $E_S - \mu_N = -1.63$ eV occurs. Applying density functional theory calculations, different microscopic diffusion mechanisms are evaluated, and the corresponding transition states are derived.

I. INTRODUCTION

With an increasing demand for efficient short wavelength light emitting diodes and lasers, many research activities have been focusing on ZnO. Its extraordinary physical properties such as a direct bandgap of 3.37 eV at room temperature, an exciton binding energy of approximately 60 meV,[1] and the availability of large wafers[2] render it suitable for opto-electronic applications. However, for most semiconductor devices, doping is essential. In view of this requirement, ZnO has a major drawback since it is afflicted with doping asymmetry. Commonly, as-grown undoped ZnO exhibits n-type conductivity, which has been ascribed to the presence of oxygen vacancies, zinc interstitials, and hydrogen.[3–10] Nevertheless, n-type conductivity can be well controlled by adding donor atoms such as Al, B, Ga, In, and Sn.[11–15]

On the other hand, previous and recent reports on p-type doping of ZnO are controversial. While some researchers have reported on ZnO with high carrier concentrations and high mobilities, others have claimed that stable p-type ZnO does not exist. The growth of stable p-type ZnO with large hole concentrations is difficult to achieve. Potential acceptors are group I elements accommodated at Zn-sites and group V elements substituting O atoms.[16,17] Although p-type doping has been attempted with many potential acceptor atoms, quite a number of studies have focused on nitrogen as the acceptor of choice since it has been suggested as an ideal candidate to achieve p-type doping.[18] Unfortunately, the doping efficiency was found to be exceedingly low.[19] This may be due to a number of reasons. Density functional theory calculations have suggested that N is a deep acceptor with an ionization energy of 0.4–1.3 eV.[20,21] In addition, the doping efficiency of nitrogen decreases due to the formation of complexes, such as NO, N_2O, N_2, transition-metal nitrogen complexes, and carbon nitrogen complexes.[20,22–27] On the other hand, it has been suggested that complex formation may also result in p-type doping with rather small ionization energies.[28] Hence, the numerous reports in the

literature show that the properties ascribed to nitrogen in ZnO are manifold and extend well beyond the simple picture of an acceptor atom. Evidently, the lattice position of nitrogen and the character of its accommodation depend on experimental conditions. This raises questions regarding the stability and diffusivity of nitrogen in ZnO.

In the past, few studies regarding nitrogen diffusion in ZnO were reported. For this purpose, N was introduced by ion implantation or diffusion from a solid source. ZnO implanted with nitrogen and indium did not show any sign of N diffusion when annealed at 800 °C.[29] On the other hand, Zhang *et al.*[30] observed the out-diffusion of nitrogen from indium doped ZnO already at temperatures of about 600 °C. However, N diffusion deeper into the volume of the host material was not observed.[30] The migration behavior of nitrogen changes when nitrogen is introduced from a solid source. When ZnO is deposited on InN, a rapid thermal anneal at 850 °C for 20 s in the presence of oxygen caused N atoms to migrate from the underlying InN layer into the ZnO layer where they acted as acceptors.[31] However, despite the importance of nitrogen diffusion in ZnO, none of these approaches provide a sound insight into the underlying mechanisms of N diffusion nor do they estimate diffusion coefficients and diffusion barriers.

In this paper, we investigate nitrogen transport in pulsed laser deposited ZnO layers by two different methods. First, we address the question whether nitrogen migration is governed by atomic or molecular diffusion by employing gas effusion experiments on ZnO doped with ^{14}N and ^{15}N isotopes. Information on the diffusivity was deduced from effusion measurements and by analyzing nitrogen concentration depth profiles measured by secondary-ion-mass spectrometry (SIMS). Finally, a microscopic model for N diffusion in ZnO and possible diffusion paths are presented.

The paper is organized as follows. The experimental details such as sample preparation and the employed methods are briefly described in Sec. II. Information on the crystalline quality of the PLD-grown samples is presented in Sec. III A. In Sec. III B, experimental evidence for monatomic nitrogen diffusion is presented, while Sec. III C addresses nitrogen diffusion coefficients that are determined from concentration depth profiles and gas effusion measurements. In Sec. IV, we discuss the implications of the data for nitrogen transport and present a model that accounts for N diffusion in ZnO. Furthermore, microscopic diffusion mechanisms are evaluated, and finally, in Sec. V, the main conclusions of this work are summarized.

II. EXPERIMENTAL DETAILS

Zinc oxide films were grown on c-axis sapphire and float zone single crystal silicon at a substrate temperature of 550 °C using pulsed laser deposition (PLD). Prior to the deposition, the substrates were subjected to a prolonged anneal to remove nitrogen. The targets were produced by cold-pressing the commercially available ZnO powder with a purity of 99.9995% and a subsequent sintering step at 950 °C for 5 h in ambient air to yield ceramic ZnO. For the deposition, a XeCl and a KrF excimer laser emitting at a wavelength of 308 and 248 nm, respectively, were used. The lasers were operated at a pulse repetition rate of 10 Hz and a laser fluence of about 2.5 J/cm^2. To incorporate nitrogen atoms into the ZnO layers, monatomic nitrogen generated in a remote plasma was added during growth. The nitrogen flow was set to 40 and 45 SCCM. To obtain stoichiometric ZnO, an oxygen gas flow was added to the remote plasma. For some secondary-ion-mass spectrometry and gas effusion measurements, $^{15}N_2$ was used as a tracer element that duplicates $^{14}N_2$ chemistry. Nitrogen concentration depth profiles were measured using secondary-ion-mass spectrometry. For calibration, a N implanted ZnO standard was used. The depth scales were acquired by measuring the depth of the sputtered craters with a mechanical stylus.

When using gas effusion measurements,[32–34] the specimens were annealed in ultrahigh vacuum with a constant heating rate, while the molecular nitrogen flux was measured with a quadrupole mass spectrometer. The relative ion current obtained from the quadrupole mass spectrometer was calibrated using the known neon flux through a capillary. Structural information was obtained from secondary-electron microscopy (SEM) and from Raman backscattering. For the latter method, a HeNe laser was used as an excitation source and the backscattering spectra were measured at room temperature.

Density functional theory calculations were performed to determine the transition barriers for likely nitrogen diffusion paths. The calculations were performed using the projector augmented plane wave approach and a super cell geometry with up to 96 atoms. The *d* electrons of Zn were treated as valence electrons. For the calculations, the GGA + *U* approximation with an onsite coulomb repulsion parameter of U–J = 4.7 eV was employed.[35,36] The plane wave cutoff amounted to 400 eV and a k-point mesh of $3 \times 3 \times 3$ was used. To determine the diffusion barriers, a modified nudged elastic band (NEB) method, namely, the climbing-image technique was employed.[37] The calculations were performed with the Vienna *ab initio* simulation package (VASP).[38,39]

III. RESULTS

The results presented in this section were obtained from Raman backscattering measurements, SEM, gas effusion, and SIMS measurements. In Sec III A, information on the crystalline quality of the samples is provided. Then, in Sec. III B, samples isotopically enriched with ^{14}N and ^{15}N are used to elucidate the fundamental migration process and address the question whether nitrogen diffuses primarily monatomic or molecular. In Sec. III C, diffusion coefficients and migration barriers are deduced from SIMS depth profiles and nitrogen effusion measurements.

A. Microscopic structure

Information on the structural properties were obtained from Raman backscattering and SEM measurements. At the Γ-point, the zone centered phonon modes are given by[40]

$$\Gamma = A_1 + 2B_1 + E_1 + 2E_2. \quad (1)$$

The E-modes are twofold degenerate, and the B modes are infrared and Raman inactive modes. Raman backscattering spectra measured on PLD-grown ZnO on sapphire and single crystal silicon (c-Si) substrates are shown in Fig. 1. The measurements were performed at room temperature. Both spectra exhibit the E_2^{low}

and E_2^{high} phonon modes at $\nu = 98$ and $436\,cm^{-1}$, respectively. Also, the mixed phonon mode at $\nu = 334\,cm^{-1}$ is visible in the spectra. Depending on the used substrate, additional phonon modes are visible that originate from the substrates. For ZnO deposited on sapphire (blue curve), these modes are marked with an asterisk. For ZnO deposited on c-Si (red curve), the TA and LO–TO phonons of c-Si are visible. In the inset of Fig. 1, a cross-sectional SEM micrograph of PLD-grown ZnO is depicted. The micrograph shows that the ZnO layer is composed of columnar grains. The results from SEM and Raman scattering confirm that the specimens are composed of columnar grains and hence are polycrystalline.

B. Monatomic nitrogen diffusion

In Fig. 2, the ion flux for the masses 44 (N_2O), 28 (N_2), 16 (O), and 32 (O_2) are plotted as a function of the annealing temperature, T. At a temperature of $T = 586\,°C$, the ion flux of N_2O, N_2, and O exhibit a pronounced peak. A second less pronounced peak is observed at $T = 838\,°C$. The data shown in Fig. 2 suggest that molecular nitrogen and nitrous oxide are formed either in the bulk or at the surface of the specimen during the gas effusion experiment. However, since the effusion peaks for N_2O, N_2, and O occur at the same temperature, a fraction of N_2 and the weak signal for atomic O are due to a dissociation reaction of nitrous oxide at the filament of the quadrupole mass spectrometer. On the other hand, molecular oxygen is detected only at annealing temperatures of $T > 950\,°C$, which is supporting the previous conclusion. Moreover, it indicates that the ZnO samples are thermally stable up to 950 °C.

To answer the question whether N_2 and N_2O are formed in the bulk or at the surface of ZnO, isotope experiments using ^{14}N and ^{15}N were performed. Sample stacks were deposited at a substrate temperature of 550 °C where the first ZnO layer was doped using ^{15}N and the second layer was doped with ^{14}N. Nitrogen concentration depth profiles were obtained from SIMS measurements and are plotted in Fig. 3. The top layer doped with ^{14}N shows a homogeneous nitrogen concentration of $\approx 1.4 \times 10^{18}\,cm^{-3}$. At a depth of about $0.5\,\mu m$, the doping source was changed to ^{15}N. The change of the doping source resulted in a steep decrease of the ^{14}N

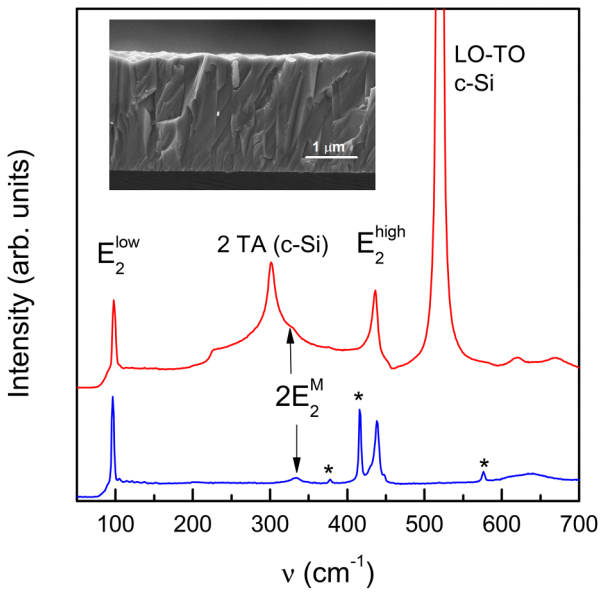

FIG. 1. Raman spectra of PLD-grown ZnO thin films. The samples were deposited on single crystal silicon (red curve) and sapphire substrates (blue curve). The 633 nm emission line of a HeNe laser was used as the excitation source. The E_2^{low} and E_2^{high} phonon modes and the mixed 2 E_2^M mode attributed to ZnO are clearly visible in the spectra. 2TA and LO–TO indicate the phonon modes from c-Si, and the asterisks show phonon modes that originate from the sapphire substrates. An SEM cross-sectional micrograph is depicted in the inset. The measurements were performed at room temperature.

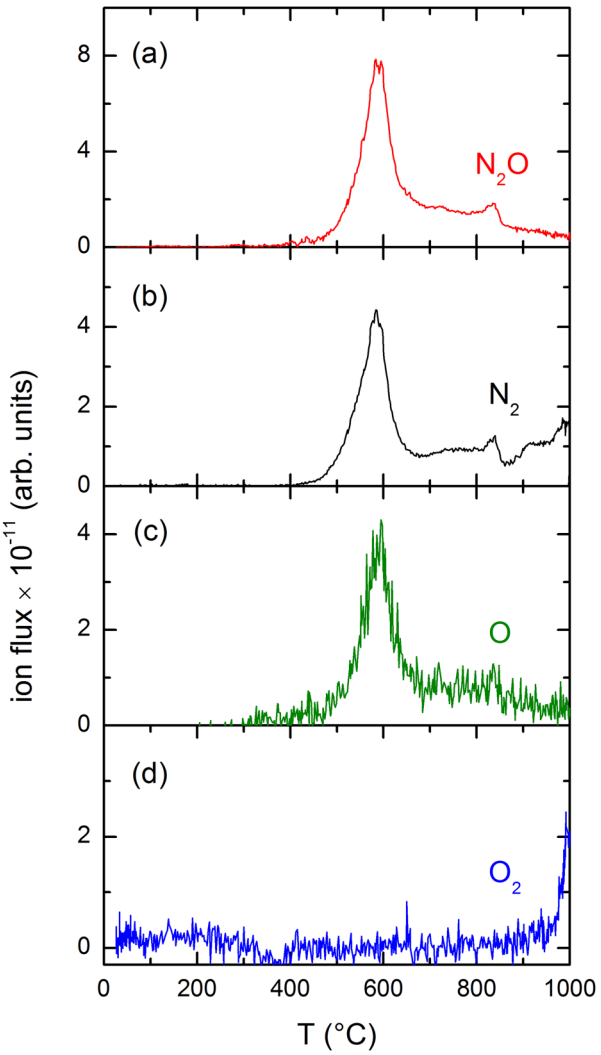

FIG. 2. The temperature dependence of the ion flux of N_2O, N_2, O, and O_2 are shown in (a), (b), (c), and (d), respectively. The ZnO sample was annealed with a heating rate of dT/dt = 20 K/min.

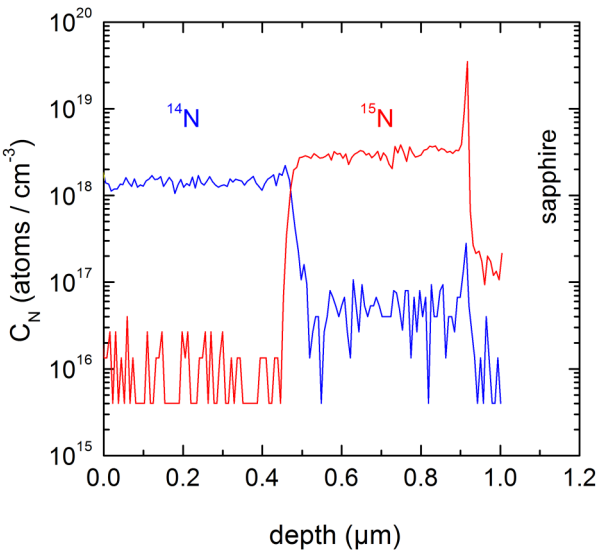

FIG. 3. Depth distribution of ^{14}N and ^{15}N in as-deposited ZnO obtained from SIMS measurements.

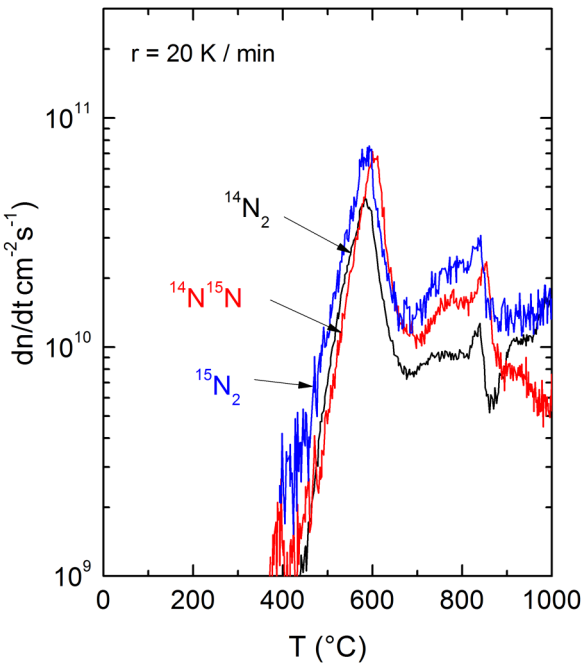

FIG. 4. Molecular nitrogen flux as a function of temperature. The ZnO sample was doped with nitrogen using a remote microwave plasma. For the first 0.5 μm isotopically enriched ^{15}N was used, while the second half of the sample was doped with ^{14}N. The depth distribution of the isotopes is shown in Fig. 3. The sample was annealed with a heating rate of 20 K/min.

depth profile and a steep increase of the ^{15}N depth profile. The bottom layer also shows a homogeneous depth distribution with a concentration of $\approx 2.6 \times 10^{18}$ cm^{-3}. The sharp decrease of the ^{14}N and ^{15}N concentrations at a depth of about 0.5 μm shows that interdiffusion of the nitrogen isotopes during the growth process can be neglected. At the interface to the sapphire substrate, a peak in the ^{15}N concentration is observed. This is an artifact of the SIMS measurement and is ascribed to a change of the lattice matrix from ZnO to sapphire.

A sample from the same deposition was placed into the gas effusion system and the molecular nitrogen flux was measured as a function of the annealing temperature, T. The sample was annealed with a heating rate of $r = 20$ K/min. In Fig. 4, the molecular flux of nitrogen is plotted as a function of T. The out-diffusion of nitrogen commences at $T \approx 400$ °C. It is important to note that the fluxes of $^{14}N_2$, $^{15}N_2$, and $^{14}N^{15}N$ are similar in value and exhibit the same temperature dependence. The nitrogen molecules can either form in the ZnO layer or at the surface of the sample. If the molecules were to form within the ZnO layer, nitrogen diffusion would be governed by molecular diffusion. However, if the molecules were to form at the surface prior to desorption into vacuum, the diffusion mechanism would be governed by atomic N diffusion. In the case of molecular N diffusion, the flux of $^{14}N^{15}N$ molecules should be significantly smaller than the flux of $^{14}N_2$ and $^{15}N_2$ molecules. While the isotopically pure molecules $^{14}N_2$ and $^{15}N_2$ could form in significant concentrations in the top and bottom half of the sample, respectively, the isotopically mixed molecule $^{14}N^{15}N$ would form only in the region where both isotopes are incorporated with high-concentrations. This region occurs at a depth of ≈ 0.47 μm and has a width of less than 40 nm (see Fig. 3). Consequently, if the molecules would form in the specimen prior to out-diffusion, the concentration, and the measured flux of $^{14}N^{15}N$ should be significantly smaller than the flux of isotopically pure nitrogen molecules. This, however, is not the case. The data show similar values for $^{14}N_2$, $^{15}N_2$, and $^{14}N^{15}N$ molecules. A comparable concentration of $^{14}N^{15}N$ to $^{14}N_2$ and $^{15}N_2$ molecules can only be obtained when nitrogen diffusion in ZnO is governed by atomic diffusion. Hence, our data clearly demonstrate that N migration is governed by atomic diffusion. N atoms diffuse through the bulk toward the ZnO surface where they form molecules prior to desorption.

C. Diffusion coefficients

1. Concentration depth profiles

Further insight into the atomic N diffusion process was obtained from post-annealing experiments of ZnO:^{14}N–ZnO:^{15}N sample stacks. Typical nitrogen concentration depth profiles of as-deposited and post-annealed samples are shown in Fig. 5. Annealing was performed at the indicated temperatures for 1 h. Atomic N diffusion is observed for annealing temperatures $T_A > 550$ °C. With increasing T_A, the ^{14}N and ^{15}N depth profiles broaden. In addition, at $T_A = 700$ °C, the ^{14}N and ^{15}N concentrations decrease from $C_{^{14}N} \approx 1.5 \times 10^{18}$ cm^{-3} and $C_{^{15}N} \approx 3 \times 10^{18}$ cm^{-3} to $C_{^{14}N} \approx 7.2 \times 10^{17}$ cm^{-3} and $C_{^{15}N} \approx 1.2 \times 10^{18}$ cm^{-3}, respectively. This indicates that the nitrogen diffusion-length is large enough for atoms to reach the surface or interface and leave the sample.

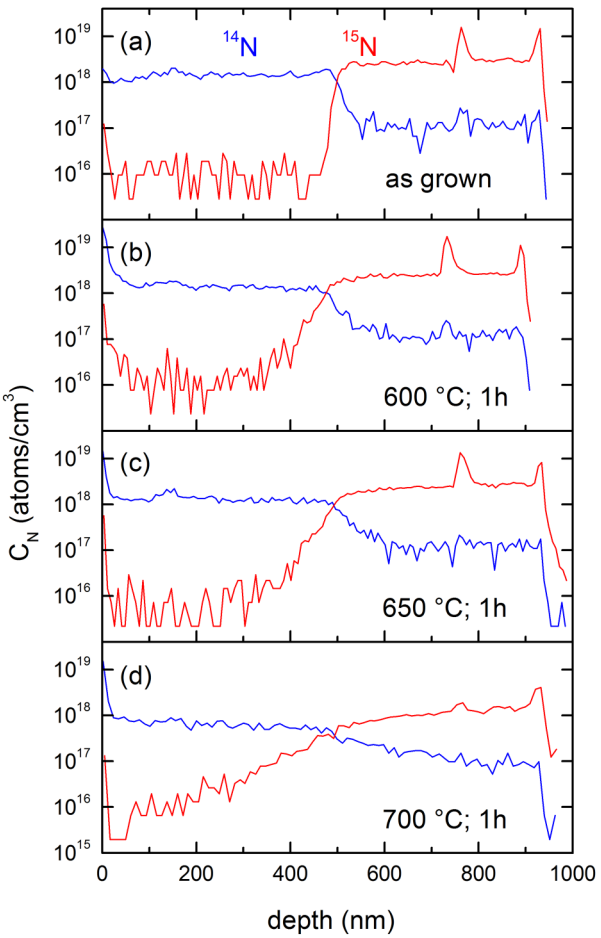

FIG. 5. ^{14}N and ^{15}N concentration vs depth in ZnO obtained from SIMS measurements. The samples were deposited at 550 °C. Doping was achieved by adding nitrogen from a remote microwave plasma. The nitrogen depth distribution in as-grown ZnO is plotted in (a). Subsequently, the specimens were annealed for 1 h at the indicated temperatures (b)–(d).

For the analysis of concentration depth profiles, a number of approaches can be used depending on the experimental boundary conditions.[41] In the past, two different models were applied to describe complex diffusion profiles in semiconductors. One model emphasizes trapping and de-trapping of the diffusing species at energetically shallow and/or deep sites.[42] This model has the advantage that it can be applied without the knowledge of specific chemical reactions that might occur in the migration process or the exact nature of participating defects and complexes. Moreover, the beauty of this model is that it allows us to determine energy barriers and, hence, provide insight into the governing migration processes solely based on the macroscopic data, namely, the concentration depth profiles.

On the other hand, diffusion can also be described by taking into account specific chemical reactions of the migrating entity in the host material.[43] Since it is difficult to determine the exact

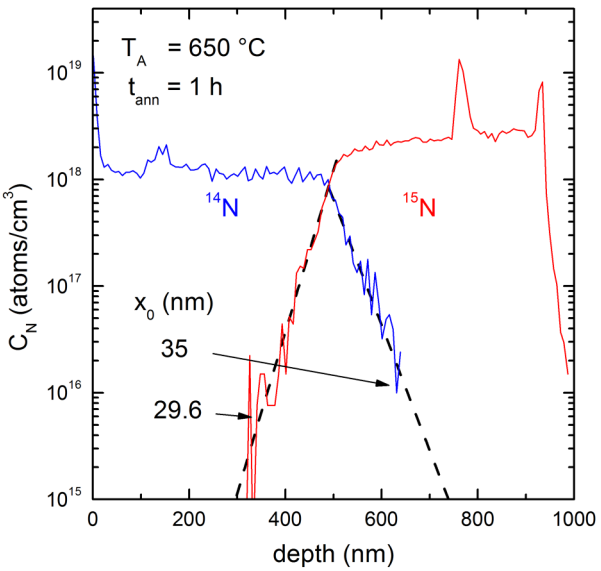

FIG. 6. ^{14}N and ^{15}N concentration vs depth in ZnO obtained from SIMS measurements. The sample was annealed at $T_A = 650$ °C for 1 h. The dashed lines indicate exponential decays with a characteristic length of $x_0 \approx 35$ and 29.6 nm for ^{14}N and ^{15}N, respectively.

reactions for a given diffusion problem, often only conceivable reactions are assumed. Moreover, for complex and manifold reactions, the analysis may become difficult. This is a shortfall of the model. However, both models have their merits and can provide insight into the microscopic diffusion mechanisms. For the given diffusion problem of nitrogen in ZnO, we decided to employ the trapping/de-trapping model since little is known about the exact structure of defects interacting with nitrogen atoms and of nitrogen-related complexes that can form in ZnO.

In Fig. 6, the nitrogen concentration depth profiles are shown for a specimen that was annealed for 1 h at a temperature of 650 °C. For both nitrogen isotopes, an exponential decrease of the nitrogen concentration is observed with a characteristic slope of $x_0 = 35$ and 29.6 nm for ^{14}N and ^{15}N, respectively. Interestingly, for $C_{^{15}N} > 10^{18}$ cm^{-3}, the ^{15}N depth profile (red curve) deviates from the exponential decrease and can be described with a complementary error function (erfc). Similar results were obtained for the other depth profiles. However, there is too little data for a conclusive fit. The functional change of the depth profiles from an erfc to an exponential decay occurs when the nitrogen concentration equals the density of traps for N atoms. According to Fig. 6, this occurs at $C_N \approx 1.4 \times 10^{18}$ cm^{-3}.

From the characteristic decay length, the diffusion coefficients were determined applying the relation

$$D = \frac{x_0^2}{4t_{\text{ann}}}. \tag{2}$$

The diffusion coefficients for ^{14}N and ^{15}N are plotted as a function of the annealing temperature, T_{ann}, in Fig. 7. For $T_{\text{ann}} \leq 650$ °C, D

is independent of the annealing temperature and a mean value of $D \approx 7.4 \times 10^{-16}$ cm^2/s is obtained. It is interesting to note that the diffusion coefficients increase by more than an order of magnitude when the samples are annealed at 700 °C.

2. Diffusion coefficients determined from effusion measurements

Deeper insight into the properties of nitrogen in ZnO, such as the total nitrogen concentration, the temperature dependence of the N evolution rates, nitrogen binding energies, and the diffusion coefficients can be obtained from effusion measurements. In order to access these parameters, a second set of samples with a higher nitrogen content was used. The increase of the N concentration was achieved by increasing the N_2 flux during deposition. All samples were grown in the same deposition run.

Nitrogen effusion data obtained for different heating rates, r, are displayed in Fig. 8. The ordinate shows the number of nitrogen atoms that leave the samples per unit temperature interval and unit surface area. The employed heating rates varied from 10 to 40 K/min. The data shown in Fig. 8 were obtained from samples that were deposited simultaneously. Out-diffusion of nitrogen commences for temperatures above 200 °C. All spectra exhibit three pronounced maxima of the nitrogen flux that shift to higher temperatures with increasing heating rate. However, the prominent peak observed at $T > 900$ °C is not directly related to nitrogen in the ZnO layers. This peak is caused by N atoms that migrate into the substrate at lower temperatures from where they are released at higher temperatures. Therefore, the peak cannot be used for the following analysis.

The nitrogen concentration, C_N, of the specimens was derived by integrating the effusion spectra and taking into account the sample thickness. In Fig. 9, C_N is plotted as a function of the heating rate. Since the specimens were grown in the same deposition, they show the same nitrogen concentration that amounts to about 7.9×10^{19} cm^{-3}. It is important to note that C_N exceeds the nitrogen concentration of the first batch of ZnO samples by more than a factor of 30 (see Figs. 5 and 6). As will be shown below, the higher N concentration results in considerably higher diffusion coefficients.

In Fig. 10, the temperature at which the nitrogen effusion rate exhibits the largest value, T_{max}, is shown as a function of the heating rate, r. With increasing heating rate, T_{max} increases from 560.7 to 611.1 °C. The increase of T_{max} is consistent with the diffusion of monatomic N from the bulk to the sample surface. Previously, a similar behavior was reported for the diffusion of hydrogen atoms in amorphous silicon[44] and ZnO.[33,34] At any given time, the nitrogen distribution in the specimens can be derived from the diffusion equation

$$\frac{\partial C(x,t)}{\partial t} = D(t)\frac{\partial^2 C(x,t)}{\partial x^2}, \tag{3}$$

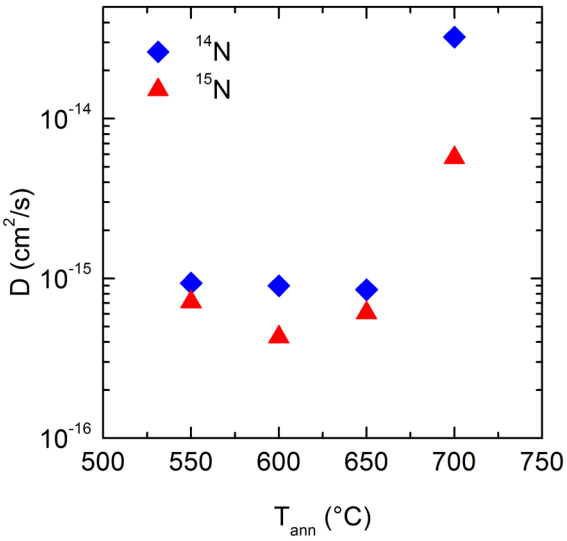

FIG. 7. Nitrogen diffusion coefficients as a function of the annealing temperature, T_{ann}, for low concentration diffusion ($C_N < 1 \times 10^{18}$ cm^{-3}). The diamonds and triangles were obtained for atomic ^{14}N and ^{15}N diffusion, respectively.

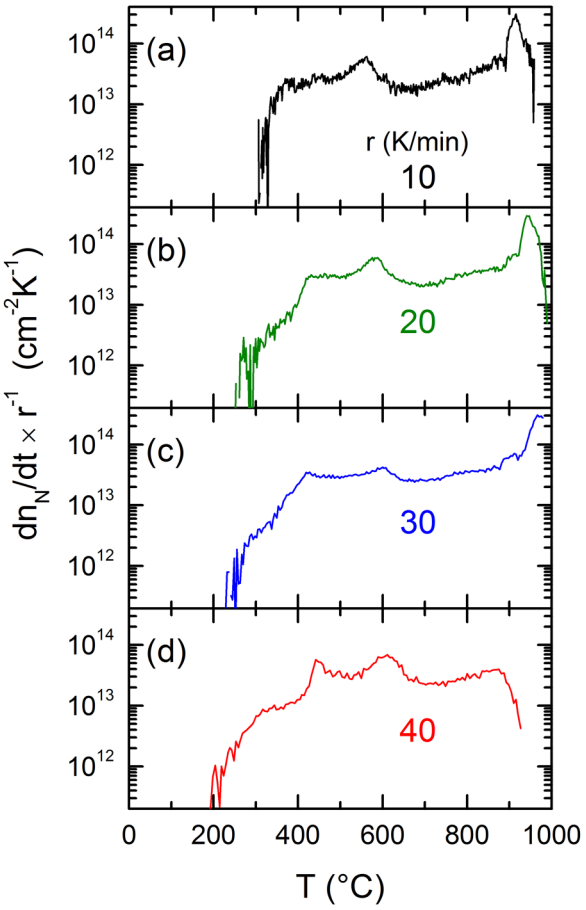

FIG. 8. Molecular nitrogen evolution rate r^{-1}dN/dt as a function of temperature. The data shown in (a)–(d) were obtained for heating rates ranging from 10 to 40 K/min.

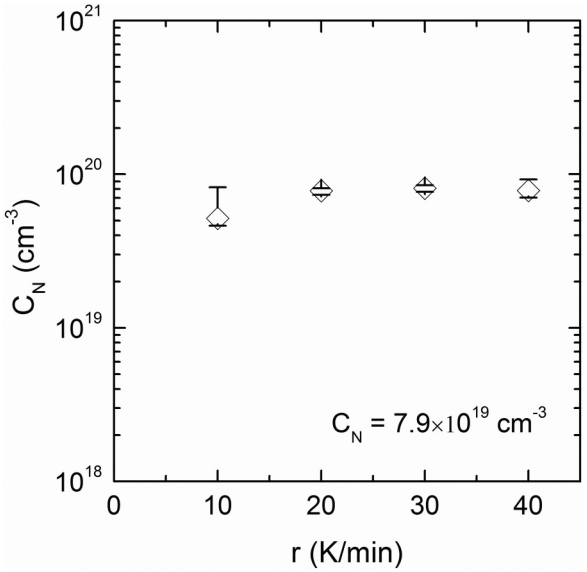

FIG. 9. Nitrogen concentration, C_N, as a function of the heating rate, r. The data were obtained from the N effusion spectra in Fig. 8.

where D represents the time dependent diffusion coefficient

$$D(t) = D_0 \exp\left(-\frac{E_A}{tk_B r}\right). \tag{4}$$

Here, E_A is the diffusion activation energy, D_0 denotes the diffusion prefactor, and k_B is the Boltzmann constant. In the as-deposited

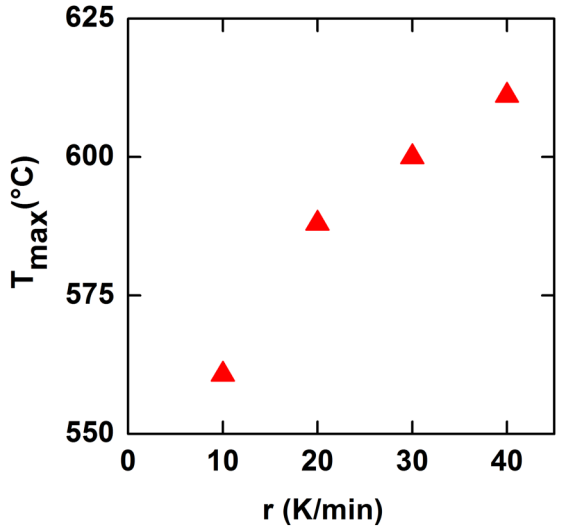

FIG. 10. Temperature of the maximum nitrogen flux, T_{max}, as a function of the heating rate, r.

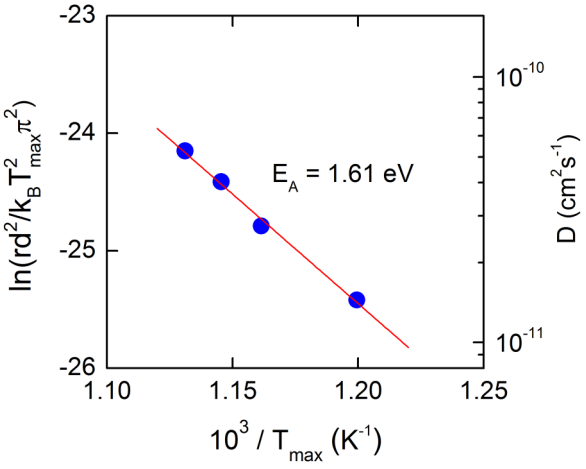

FIG. 11. $\ln(rd^2/k_B T_{max}^2 \pi^2)$ and the resulting diffusion coefficients, D, as a function of $10^3/T_{max}$ for the data shown in Fig. 10.

samples, the nitrogen concentration is constant with depth. During the effusion measurement, the temperature increases linearly with time. With these boundary conditions, Eq. (2) can be solved to deduce the diffusion coefficients from gas effusion measurements,[44]

$$\ln\left(\frac{rd^2}{k_B T_{max}^2 \pi^2}\right) = \ln\left(\frac{D_0}{E_A}\right) - \frac{E_A}{k_B T_{max}} = \ln\left(\frac{D}{E_A}\right). \tag{5}$$

Using this equation, the temperature dependence of the diffusion coefficient can be determined by measuring nitrogen effusion as a function of the sample thickness, d, or as a function of the heating rate, r,

In Fig. 11, the values obtained from $\ln(rd^2/k_B T_{max}^2 \pi^2)$ are plotted as a function of the inverse temperature, T_{max}. A least-squares fit to the data yielded an activation energy of $E_A = 1.61$ eV (solid line). From the data shown in Fig. 11, the diffusion coefficients were determined according to

$$D = D_0 \exp\left(-\frac{E_A}{k_B T}\right). \tag{6}$$

An Arrhenius plot of the diffusion coefficient is shown in Fig. 11. The values have to be compared to the diffusion coefficients obtained from the nitrogen concentration depth profiles (Fig. 7). It is obvious that there is a difference in the diffusion mechanisms for low and high nitrogen concentrations. For low N concentration the diffusion coefficient is constant with temperature up to 650 °C and amounts to $D \approx 7.4 \times 10^{-16}$ cm^2/s. On the other hand, for high N concentration an Arrhenius behavior is observed with an activation energy of 1.61 eV (Fig. 11) and the diffusion coefficients are about 6 orders of magnitude larger.

IV. DISCUSSION

The experimental data presented in Sec. III show that the microscopic diffusion mechanism in ZnO is governed by atomic nitrogen migration. This important insight will be used to develop a microscopic model for N diffusion in ZnO and to identify possible diffusion paths. This section is divided into three parts. First, the experimental data are described in terms of a two-band model (Sec. IV A). Key parameters such as the energy depth and trap concentration are estimated from the temperature dependence of the diffusion and from the nitrogen effusion data. The character of the deep traps is discussed in Sec. IV B. Finally, different microscopic diffusion mechanisms are evaluated, and the corresponding transition states are calculated (Sec. IV C).

A. Nitrogen density of states

A number of properties of nitrogen diffusion in ZnO can be determined from the experimental data presented above. For the diffusion process, it is reasonable to assume that nitrogen atoms migrate between minimum energy positions by surmounting a barrier between sites at a saddle point. Although the PLD deposited films exhibit a polycrystalline nature with a c-axis surface orientation, the migration saddle point represented by the energy E_S is considered to be roughly constant throughout the ZnO layer. Below E_S nitrogen trapping sites are located that trap and release N during the diffusion process. On the time scale of a typical diffusion experiment, nitrogen equilibrates in these shallow traps. However, depending on the exact microscopic migration path and the charge state of N, some minor variations on the corresponding energy levels have to be taken into account. The microscopic diffusion mechanisms are discussed in detail below (see Sec. IV C).

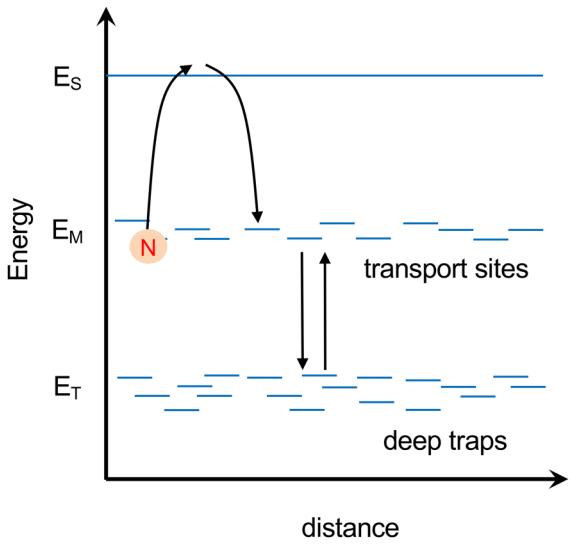

FIG. 12. Two-level model for nitrogen migration in ZnO. The N transport sites are represented by E_M and E_S denotes the migration saddle point. Separated in energy at E_T are deep trapping sites for nitrogen.

Separated in energy from the shallow traps are deep traps at an energy E_T. Nitrogen atoms that are trapped in these states also participate in the diffusion process but on very long timescales. Subsequently, the corresponding diffusion coefficients are about six orders of magnitude smaller (see Fig. 7). Similar to hydrogen diffusion in ZnO, nitrogen migration can be described in terms of a trapping and release mechanism from a density of binding-site energies over barrier energies. The two-level model is schematically depicted in Fig. 12. Hence, nitrogen diffusion is described by Eq. (6) where the activation energy is given by

$$E_A = \begin{cases} E_S - E_M & \text{when } N_T + N_M > C_N > N_T, \\ E_S - E_T & \text{when } C_N < N_T. \end{cases} \quad (7)$$

Here, N_T and N_M denote the number of occupied deep trapping and transport sites, respectively. E_M and E_T represent the energy of the transport sites and deep traps, respectively. In order to derive the energetic positions of the deep traps and the transport sites from the experimental data, the diffusion pre-factor, D_0, has to be independent of the experimental parameters. Moreover, it has to reflect the microscopic diffusivity of nitrogen in ZnO. Extrapolating the Arrhenius plot of the diffusion coefficients (Fig. 11) to $1/T = 0$ yields a prefactor of $D_0 \approx 7.4 \times 10^{-4}\,\mathrm{cm^2\ s^{-1}}$. On the other hand, the value of the diffusion prefactor can be estimated from Ref. 45,

$$D_0^T = \frac{1}{N_{\mathrm{sites}}} \nu a^2, \quad (8)$$

where N_{sites} corresponds to the number of nearest neighbor sites for N migration, ν is the attempt frequency, and a denotes the mean-free path. Two prominent diffusion mechanisms that will be described in detail below are vacancy and N–O dumbbell promoted nitrogen migration. In both cases, the number of nearest neighbor sites amounts to $N_{\mathrm{sites}} = 4$. Using values of $a \approx 3.2$ Å and $\nu = 10^{13}\,\mathrm{s^{-1}}$ the diffusion prefactor can be estimate to $D_0^T \approx 2.6 \times 10^{-3}\,\mathrm{cm^2\ s^{-1}}$. This value is about one order of magnitude larger than D_0 determined from the experimental data and will later be used to determine the correct position of the N trapping sites for high-concentration diffusion. On the other hand, for deep traps, D is independent of temperature (Fig. 7). To assign an energy value to E_T the nitrogen chemical potential can be derived from the diffusion coefficients using the relation

$$E_S - \mu_N(T) = -k_B T \ln\left(\frac{D}{D_0^T}\right). \quad (9)$$

For the calculation, the theoretically derived prefactor was used. For the accuracy of this approach, it is important to note that the energy depends logarithmically on the diffusion prefactor. Thus, even an error of one order of magnitude will change the energy values only by less than 0.1 eV. In Fig. 13, the position of the N chemical potential is plotted as a function of temperature. For high-concentration diffusion (solid symbols), a constant value of $E_S - \mu_N \approx -1.36$ eV is obtained. This indicates that the density-of-states is high and the chemical potential is pinned. $E_S - \mu_N$ has to be compared to the activation energy derived from the data in Fig. 11. Both values should be approximately equal,

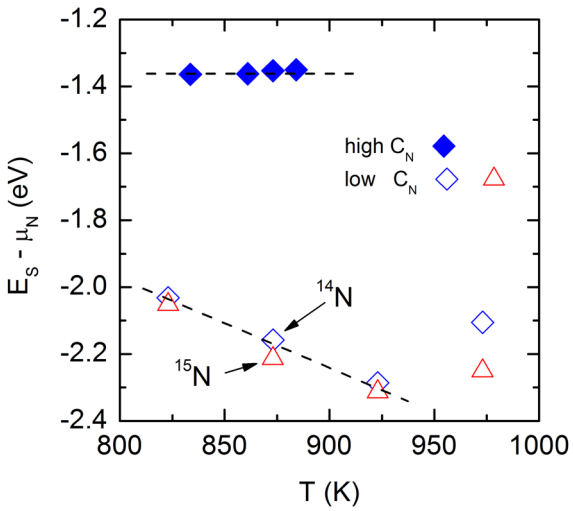

FIG. 13. Nitrogen chemical potential, E_S–μ_N, as a function of temperature for high (full symbols) and low N concentration diffusion (open symbols).

however, E_A determined from the Arrhenius plot is deeper in energy by 0.25 eV. This is related to the diffusion prefactor. From the experimental data, a prefactor of $D_0 \approx 7.4 \times 10^{-4}$ cm^2 s^{-1} was obtained, while the theoretically derived value amounts to $D_0^T \approx 2.6 \times 10^{-3}$ cm^2 s^{-1}. Therefore, the position of the chemical potential, E_S–μ_N, provides a more accurate value.

For low concentration diffusion (open symbols in Fig. 13), μ_N shifts deeper in energy with increasing temperature with a rate of 2.8 meV/K. Commonly, the chemical potential shifts away from high density-of-states toward energies where the density-of-states is low. According to the data shown in Fig. 13, this suggests that the density-of-states is high above the N chemical potential and μ_N shifts toward a minimum of the density-of-states that occurs deeper in energy.

The position of the nitrogen chemical potential can also be determined from the nitrogen effusion data using the relation[46]

$$E_S - \mu_N = -k_B T \ln\left(\frac{dn_{N_2}/dt}{F_0}\right), \tag{10}$$

where dn_{N_2}/dt is the molecular nitrogen flux, the prefactor is given by $F_0 \approx 2\nu N_S a/d$, and the number of surface states amounts to $N_S \approx 10^{15}$ cm^{-2}. Equation (10) can be used to calculate the N chemical potential as a function of the nitrogen concentration, C_N. The analysis was performed for the effusion data shown in Figs. 4 and 8.

For high N concentration diffusion ($C_N > 1 \times 10^{18}$ cm^{-3}), the position of the N chemical potential as a function of C_N is plotted in Fig. 14. The data were derived from the effusion spectra shown in Fig. 8. At a nitrogen concentration of ≈ 5–8×10^{19} cm^{-3}, the nitrogen chemical potential resides at E_S–$\mu_N = -0.5$ to -0.6 eV and quickly shifts further away from the N transport sites until a plateau is reached at E_S–$\mu_N = -1.3$ eV. This value is in good agreement with the position of the N chemical potential of E_S–$\mu_N = -1.36$ eV that was obtained from the diffusion coefficients for high N concentration diffusion (see full diamonds in Fig. 13). Pinning of the chemical potential occurs when the density of states is high. In the case of nitrogen, this indicates that N atoms are accommodated in the host lattice with binding energies that correspond to the position of the plateau energies. As the nitrogen content decreases further to $C_N < 5 \times 10^{18}$ cm^{-3}, the chemical potential approaches a constant value of E_S–$\mu_N \approx -2.1$ eV.

For low N concentration diffusion ($C_N < 1 \times 10^{18}$ cm^{-3}), the chemical potential shows a similar behavior (Fig. 15). For clarity, only one curve is shown. At a nitrogen concentration of $\approx 10^{18}$ cm^{-3}, the nitrogen chemical potential resides at E_S–$\mu_N = -1.18$ eV and quickly shifts further away from the H transport sites until a first plateau is reached E_S–$\mu_N = -1.64$ eV. A second plateau is observed at E_S–$\mu_N = -2.44$ eV. Finally, for $C_N < 10^{17}$ cm^{-3}, the N chemical potential approaches a value of about -3 eV.

A comparison to the data shown in Fig. 13 (open symbols) reveals a difference in E_S–μ_N of about 0.41 to 0.14 eV for the samples annealed at $T = 823$ and 973 K, respectively. It is very likely that the small discrepancy is due to subtle distinctions of the two experiments: (i) During the diffusion experiments C_N remains constant and only little nitrogen is lost at the highest annealing temperature. (ii) There is a pronounced difference in the thermal load and its change with time for the two experiments. For the diffusion experiments, the specimens are kept at a desired temperature for 1 h and are rapidly cooled to room temperature, subsequently. On the other hand, in the effusion experiment, the samples are annealed with a constant heating rate until the final temperature is reached. Finally, when the effusion measurement is finished, the

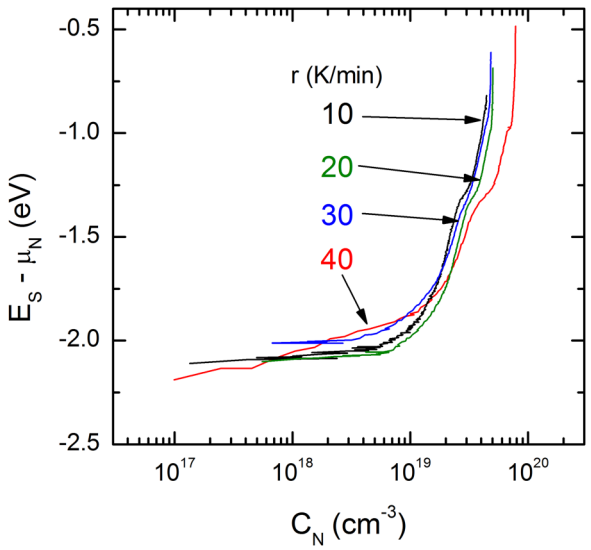

FIG. 14. Nitrogen chemical potential, E_S–μ_N, as a function of the nitrogen concentration for high N concentration diffusion ($C_N > 10^{18}$ cm^{-3}). The values were derived from the effusion data shown in Fig. 8. Details are described in the text.

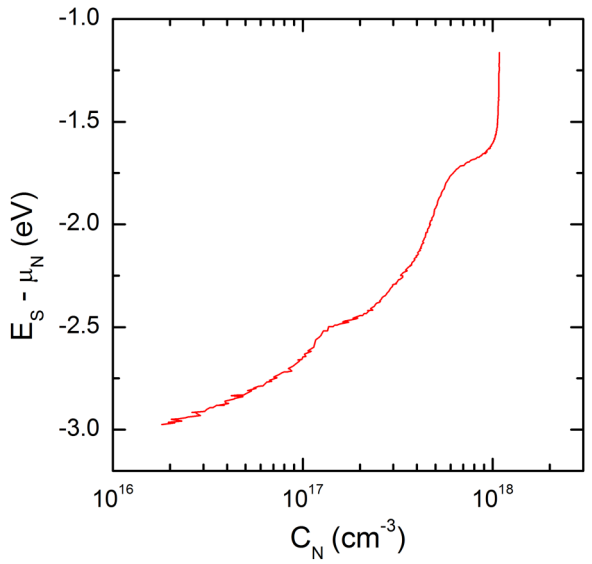

FIG. 15. Nitrogen chemical potential, E_S–μ_N, as a function of the nitrogen concentration for low N concentration diffusion ($C_N < 10^{18}$ cm^{-3}). The values were derived from the effusion data shown in Fig. 4. For clarity, only one set of data is shown. Details are described in the text.

samples are depleted of nitrogen. This manifests itself in a pronounced decrease of C_N to about 10^{15} cm^{-3}. Accordingly, the N chemical potential decreases to a value of E_S–$\mu_N \approx 3$ eV (see Fig. 15).

The effusion data can be further analyzed to derive a density-of-states distribution for nitrogen in ZnO. The total nitrogen concentration is given by

$$C_N = \int N_N(E) f(E, T, \mu_N) dE, \tag{11}$$

where N_N is the nitrogen density-of-states and $f(E,T,\mu_N)$ is the occupation function. The N density-of-states distribution can be derived from Eq. (11) by partial differentiation. At $E = \mu_N$, the partial derivative $\partial f(E, T, \mu_N)/\partial \mu_N$ peaks. Thus, the density-of-states for N atoms in ZnO can be estimated by[46]

$$N_N(\mu_N) \approx \frac{\partial C_N}{\partial \mu_N}. \tag{12}$$

The nitrogen density-of-states distributions obtained for ZnO with $C_N > 10^{18}$ cm^{-3} are shown in Fig. 16. Independent of the heating rate, all samples show two peaks. Looking at the mean values, the peaks are located at E_S–$\mu_N \approx -0.93$ eV and ≈ -1.26 eV. The more pronounced peak in the N density-of-states occurs at E_S–$\mu_N \approx -1.26$ eV, which is in good agreement with the position of the N chemical potential determined from the diffusion coefficients for high N concentration diffusion (see full diamonds in Fig. 13). This value corresponds to the energy of the transport sites with respect to the migration saddle point. Furthermore, the majority of the N atoms reside in transport sites.

For $C_N < 10^{18}$ cm^{-3}, the N density-of-states distribution looks different. In Fig. 17, the result for the mixed isotope molecule $^{14}N^{15}N$ is shown in comparison to the data obtained for $C_N > 10^{18}$ cm^{-3}. The density-of-states distributions for $^{14}N_2$ and $^{15}N_2$ are identical but they were omitted for clarity. For low N concentrations, a pronounced peak is observed at E_S–$\mu_N = -1.63$ eV (red curve in Fig. 17). Compared to the N density-of-states for high N concentrations, this peak is deeper in energy by about 0.34 eV. Further away from the saddle point, two smaller peaks appear in the density-of-states distribution at about E_S–$\mu_N = -2.17$ and -2.4 eV. According to SIMS data (see Figs. 5 and 6), N diffusion for $C_N < 10^{18}$ cm^{-3} (red curve) is trap limited. Hence, all three peaks have to be assigned to deep traps for nitrogen.

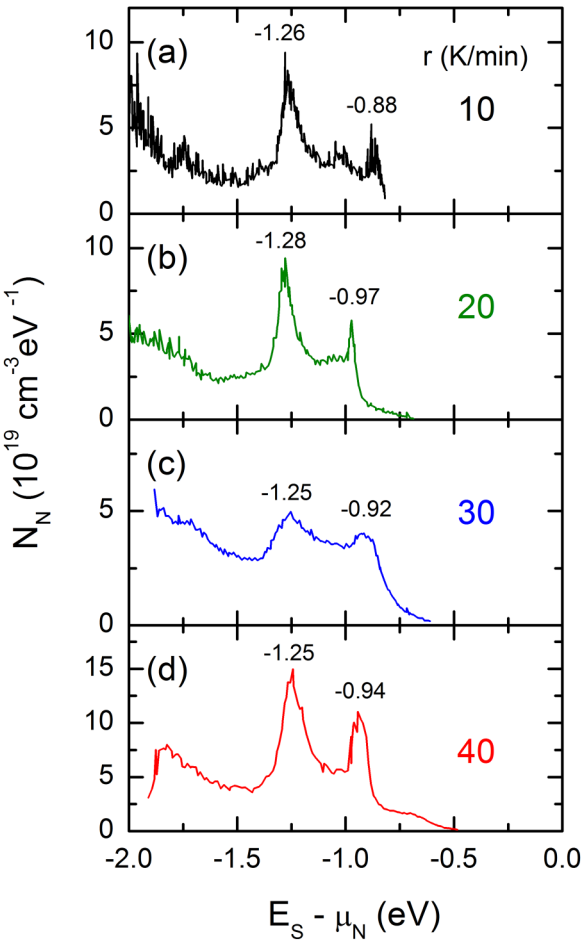

FIG. 16. Nitrogen density-of-states distribution in ZnO for high N concentrations ($C_N > 10^{18}$ cm^{-3}). The data were derived by applying Eq. (12) to the effusion spectra shown in Fig. 8. The positions of the peaks with respect to the migration saddle point, E_S, are denoted in the figure. r is the heating rate of the effusion measurements that amounted to 10 (a), 20 (b), 30 (c), and 40 K/min (d).

A characteristic property of low N concentration diffusion is the temperature independence of the diffusion coefficient (see Fig. 7). However, at the highest annealing temperature of 700 °C, an increase of D by more than one order of magnitude was observed. This increase is directly related to the nitrogen density of states (red curve in Fig. 17). The highest peak resides at $E_S - \mu_N = -1.63$ eV and contains a N concentration of about 4.4×10^{17} cm^{-3}. The temperature required to activate these N atoms can be calculated from the diffusion coefficients that were determined by applying Eq. (1) to the SIMS depth profiles. Solving Eq. (9) for T yields

$$T = -\frac{E_S - \mu_N}{k_B \ln \frac{D}{D_0^T}}. \tag{13}$$

At the highest annealing temperature, the diffusion coefficients amount to $D = 5.7 \times 10^{-15}$ and 3.2×10^{-14} cm^2/s for ^{15}N and ^{14}N, respectively (see Fig. 7). Hence, to thermally activate N atoms with a binding energy of 1.63 eV a temperature of $T = 704.7$ and 753.1 K for ^{15}N and ^{14}N is required. This is in good agreement with the pronounced increase of the diffusion coefficient for an annealing temperature of $T_A = 700$ °C (see Fig. 7).

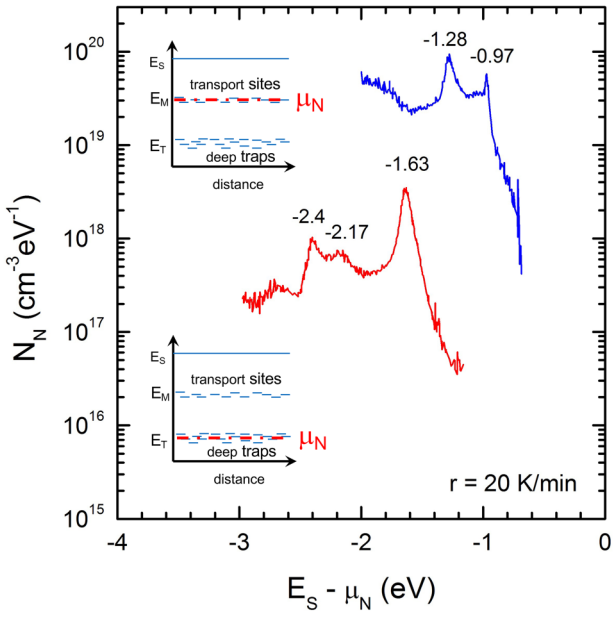

FIG. 17. Comparison of the nitrogen density-of-states distribution in ZnO for low (red curve) and high (blue curve) nitrogen concentration. The data for $C_N < 10^{18}$ cm^{-3} were obtained from the effusion data shown in Fig. 4. For clarity, only the distribution for $^{14}N^{15}N$ is plotted. The data for the other nitrogen molecules ($^{14}N_2$ and $^{15}N_2$) show the same density-of-states distribution. The data for $C_N > 10^{18}$ cm^{-3} were replotted from Fig. 16(b), where the specimen was annealed with a heating rate of 20 K/min. The sketches show the position of the nitrogen chemical potential for high and low N concentrations.

B. Character of the deep traps

The origin of the deep trapping sites for nitrogen is difficult to determine. However, an analysis of the spatial concentration depth profiles obtained from SIMS measurements can provide further details of their character. When the nitrogen concentration is comparable to or smaller than the concentration of deep traps, N_T, the migration is dominated by these traps and the diffusion depth profiles exhibit an exponential decay. For N diffusion in ZnO, the concentration of deep traps amounts to $N_T \approx 1 \times 10^{18}$ cm^{-3}. The slope of the exponential decay indicates the mean-free path for low-concentration diffusion and is given by[47]

$$x_0 = (4\pi r_C N_T)^{-\frac{1}{2}}. \tag{14}$$

Using this equation, the capture radius, r_C, can be calculated. From the SIMS depth profiles, a mean value of $x_0 = 32.3$ nm is obtained that yields a capture radius of $r_C = 0.076$ nm. It is interesting to note that similar small capture radii were reported for hydrogen diffusion in amorphous and polycrystalline silicon.[42,48] The rather small value of r_C for nitrogen capture does not allow a direct conclusion on the type of nitrogen traps.

Microscopic identification of deep N traps is difficult. It is conceivable that N atoms can form complexes with trace elements. The most common impurities in high purity ZnO powder are calcium (Ca), iron (Fe), manganese (Mn), and sodium (Na). The concentrations of these trace elements are in the sub-ppm range.[49] The impurities replace Zn in the lattice and depending on their chemical nature act as donors or acceptors. In addition, Fe and Mn doping of ZnO is used to obtain dilute magnetic semiconductors.[50–53] However, the concentration of the trace metals is about two orders of magnitude lower than the number of deep nitrogen traps in ZnO. Therefore, the trace elements cannot solely account for the concentration of deep N traps.

Another possible trapping site for nitrogen is oxygen. Fourier transform infrared (FT-IR) measurements performed on highly N-doped ZnO samples revealed local vibrational modes that are related to N–O stretching vibrations.[22] A further possible element that can trap N atoms is hydrogen, which is always present in semiconductors. In single crystal ZnO grown at temperatures ≥ 900 °C residual hydrogen concentrations between 5.2×10^{16} and 3.6×10^{18} cm^{-3} have been reported.[34] Clear evidence for the formation of N–H complexes in chemical vapor transport grown specimens using ammonia as transport gas was obtained from FT-IR measurements. The N–H complex is thermally stable up to 700 °C.[54]

Finally, molecular nitrogen might be involved to some degree. Although nitrogen diffusion is governed by atomic diffusion (see Sec. III A), some N_2 molecules might form in the bulk. However, the fraction of N atoms that form molecules can no longer participate in the atomic diffusion process by de-trapping or dissociation because of the high chemical stability of the N_2 molecule. Consequently, molecular nitrogen does not contribute to the deep traps for N in ZnO.

C. Diffusion paths

At high nitrogen concentrations ($C_N > 1 \times 10^{18}$ cm^{-3}), diffusion takes place between minimum energy positions by surmounting the barrier between sites at a saddle point. In the following, two microscopic models will be discussed that can account for atomic nitrogen diffusion and are consistent with our experimental data.

A microscopic mechanism for atomic diffusion that is encountered in numerous materials is vacancy mediated diffusion. Migration occurs when a substitutional N atom switches its lattice place with an adjacent oxygen vacancy (O_V). The initial and final atomic positions of an N atom (blue) that switches its place with an adjacent O_V are depicted in Fig. 18(a). To determine the minimum energy path and the saddle point for the vacancy mediated diffusion mechanism, the climbing-image nudged elastic band method was employed.[37] The calculations were performed for neutral and negatively charged nitrogen atoms. In Fig. 18(b), the change of the total energy, ΔE, is plotted as a function of the position of the N atom. For both charge states of the N atom, two maxima are obtained. From a symmetry point of view, the maxima should have the same energy value. But for both charge states, the maximum at the right hand is about 30 and 50 meV higher for N^-–O_V and N^0–O_V, respectively. It is conceivable that this is due to a numerical error of the calculations. However, it is interesting to note that the saddle point for vacancy mediated N diffusion is about $E_B = 1.65$ and 1.0 eV above the minimum energy position; e.g., the substitutional oxygen site, N_O, for N^-–O_V and N^0–O_V, respectively. The larger value is in good agreement with the experimental results for low N concentration diffusion (see Fig. 17) and a similar barrier height for neutrally charged N was reported by Zhang *et al.*, recently.[30] This would imply that O_V sites act as deep traps for nitrogen. However, substitutional nitrogen acts as an acceptor and, therefore, the diffusing species will be negatively charged. For N^-–O_V, the barrier height amounts to $E_B = 1.0$ eV. This energy value is too low for trap limited diffusion. Consequently, N diffusion via oxygen vacancies can be regarded as one possible mechanism for high N concentration diffusion (see Figs. 13 and 17).

For a second microscopic diffusion mechanism, the oxygen dumbbell complex[55] was revisited. Substituting one of the two O atoms with nitrogen forms a stable N–O dumbbell [see Fig. 19(a)]. The initial, one intermediate, and the final positions of nitrogen diffusing via a dumbbell complex are shown in Fig. 19(a). The intermediate configuration corresponds to the transition state and requires the surmounting of a saddle point energy of $E_B = 1.32$ and

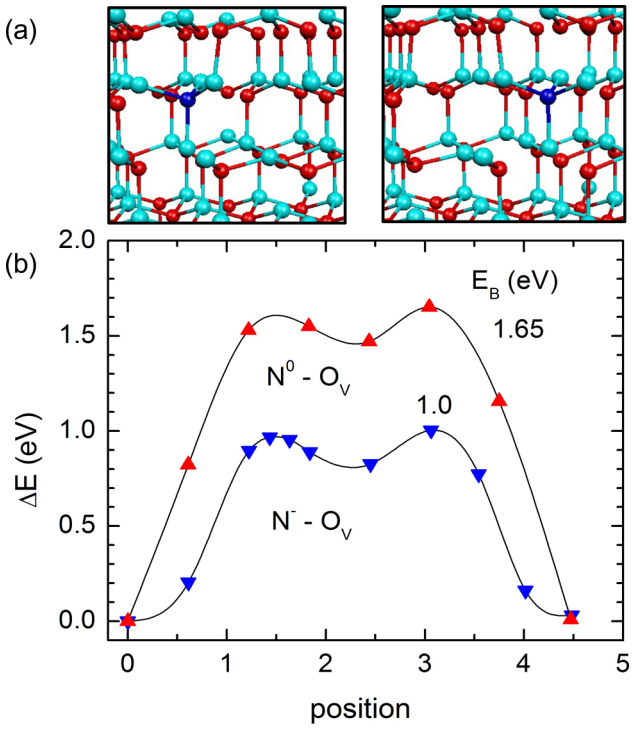

FIG. 18. Vacancy mediated nitrogen diffusion in ZnO. The initial and final positions of the N atom (blue) are shown in (a). Oxygen and zinc atoms are depicted in red and turquoise, respectively. (b) shows the change of the total energy as the N atom moves from its initial position to the vacancy. The up and down pointing triangles represent the diffusion barrier for neutral and negatively charged nitrogen, respectively.

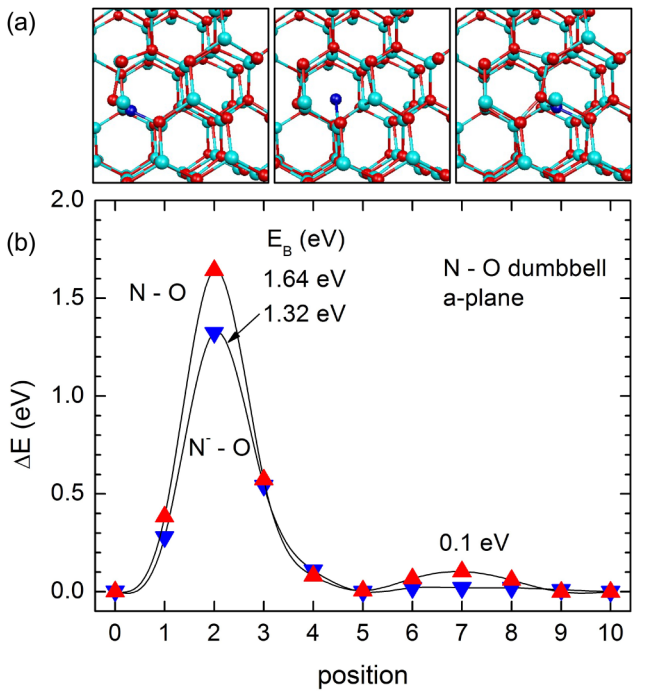

FIG. 19. Nitrogen diffusion along the a-plane of ZnO via the dissociation and formation of N–O dumbbells. (a) shows the initial, intermediate, and final positions of the diffusing N atom. The intermediate position corresponds to the transition state. (b) shows the change of the total energy as the N atom moves from its initial to its final position. The up and down pointing triangles represent the diffusion barrier for neutral and negatively charged nitrogen, respectively.

1.64 eV for N^- and N^0, respectively [see Fig. 19(b)]. When the N atom reaches the minimum energy at position 5, it forms an N–O dumbbell again [see Fig. 19(a)]. However, this position is not identical to the starting configuration since the N atom resides to the left of the O atom. In order to attain the same configuration as the starting conditions, the N–O dumbbell needs to rotate by about 180°. Interestingly, this requires only very little energy for the neutral N atom, and for the negatively charged N atom, the barrier vanishes.

Dumbbell assisted diffusion can also occur along the c-axis. The initial and final atom configurations are depicted in Fig. 20(a). The minimum energy path to overcome the saddle point is plotted in Fig. 20(b) for neutral and negatively charged nitrogen. The diffusion barrier amounts to $E_B = 1.36$ and 1.75 eV for N^- and N^0, respectively. The additional rotation of the dumbbell was omitted, since the rotation of the dumbbell requires only ≈0.1 eV for N^0, and the rotational barrier disappears for negatively charged nitrogen.

The investigated microscopic migration mechanisms have in common that their energy barriers do not differ much. For N^-, the diffusion barrier is always considerably smaller than for N^0. Assuming that most nitrogen atoms are accommodated as acceptors their charge state will be N^-. However, p-type conductivity was not observed in our samples. This is mainly due to the low N content, which results in an increase in the resistivity of the samples but is too low to compensate for all acceptors of the typically n-type ZnO. Hence, our data suggest that under the experimental conditions presented here nitrogen diffuses in the negative charge state. For N^- diffusion, the barrier energy amounts to $E_B = 1.0$–1.36 eV, which is reasonably close to the experimental values of 1.26–1.36 eV. This suggests that the three microscopic diffusion mechanisms are of high importance for N transport. Most likely, these mechanisms are the dominant diffusion processes for N in ZnO.

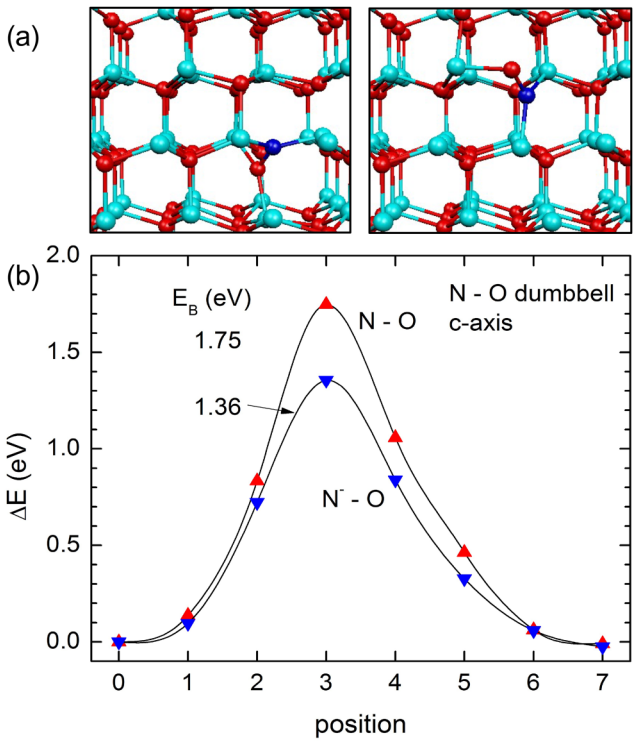

FIG. 20. Nitrogen diffusion along the c-axis of ZnO via the dissociation and formation of N–O dumbbells. (a) shows the initial and final positions of the diffusing N atom. The change of the total energy is plotted in (b) as the N atom moves from its initial to its final position. The up and down pointing triangles represent the diffusion barrier for neutral and negatively charged nitrogen, respectively.

V. SUMMARY

In summary, we have presented a detailed investigation of nitrogen diffusion in ZnO. Employing SIMS and gas effusion measurements on ZnO samples doped with ^{14}N and ^{15}N isotopes revealed that nitrogen migration is governed by atomic diffusion. For low N concentration diffusion ($C_N < 1 \times 10^{18}$ cm^{-3}), the nitrogen depth profiles exhibit an exponential decay with depth, and the diffusion coefficient is independent of the annealing temperature. For high-concentration diffusion ($C_N > 1 \times 10^{18}$ cm^{-3}), D is thermally activated with an activation energy of 1.61 eV. However, the slope of the Arrhenius plot does not correspond to the position of the chemical potential. Using the theoretical diffusion prefactor, the position of the N chemical potential was derived at E_S–$\mu_N = -1.36$ eV. Nitrogen diffusion in ZnO can be described by a two-level model, where N atoms migrate between minimum energy positions by surmounting a barrier between sites at a saddle point. Separated in energy from the shallow traps are deep traps with a concentration of $N_T \approx 1 \times 10^{18}$ cm^{-3}. The position of the N chemical potential was estimated from the SIMS data. For high-concentration diffusion, a value of E_S–$\mu_N \approx 1.36$ eV was obtained, while for low concentration diffusion a shift of μ_N away from the transport sites was observed with increasing temperature with a rate of 2.8 meV/K. The gas effusion data were analyzed to derive the nitrogen density-of-states distribution. Specimens with $C_N > 1 \times 10^{18}$ cm^{-3} exhibit two pronounced peaks that are located at an average energy of E_S–$\mu_N = -0.93$ eV and E_S–$\mu_N = -1.26$ eV. On the other hand, samples with a low N concentration ($C_N < 1 \times 10^{18}$ cm^{-3}) show a different density-of-states distribution with a dominant peak located at E_S–$\mu_N = -1.63$ eV. Microscopic diffusion mechanisms comprising vacancy and dumbbell mediated diffusion were evaluated using density functional theory calculations to determine the transition barriers. For neutral N diffusion, the barrier energy amounts to $E_B = 1.64$–1.75 eV, while for negatively charged nitrogen, the transition barriers decreased to $E_B = 1.0$ and 1.36 eV for vacancy and dumbbell mediated diffusion, respectively.

ACKNOWLEDGMENTS

The authors thank C. Klimm for providing the SEM micrographs.

AUTHOR DECLARATIONS

Conflict of Interest

The authors have no conflicts to disclose.

DATA AVAILABILITY

The data that support the findings of this study are available within the article.

REFERENCES

[1]Y. Segawa, H. D. Sun, T. Makino, M. Kawasaki, and H. Koinuma, Phys. Status Solidi A **192**, 14 (2002).
[2]K. Maeda, M. Sato, I. Niikura, and T. Fukuda, Semicond. Sci. Technol. **20**, S49 (2005).
[3]L. Liu, Z. Mei, A. Tang, A. Azarov, A. Kuznetsov, Q. K. Xue, and X. Du, Phys. Rev. B **93**, 235305 (2016).
[4]E. Scharowsky, Z. Phys. **135**, 318 (1953).
[5]S. E. Harrison, Phys. Rev. **93**, 52 (1954).
[6]E. Mollwo, Z. Phys. **138**, 478 (1954).
[7]D. G. Thomas and J. J. Lander, J. Chem. Phys. **25**, 1136 (1956).
[8]D. G. Thomas, J. Phys. Chem. Solids **3**, 229 (1957).
[9]A. Hausmann and B. Schallenberger, Z. Phys. B **31**, 269 (1978).
[10]C. G. Van de Walle, Phys. Rev. Lett. **85**, 1012 (2000).
[11]B. E. Sernelius, K.-F. Berggren, Z.-C. Jin, I. Hamberg, and C. G. Granqvist, Phys. Rev. B **37**, 10244 (1988).
[12]W. W. Wenas, A. Yamada, K. Takahashi, M. Yoshino, and M. Konagai, J. App. Phys. **70**, 7119 (1991).
[13]B. M. Ataev, A. M. Bagamadova, A. M. Djabrailov, V. V. Mamedov, and R. A. Rabadanov, Thin Solid Films **260**, 19 (1995).
[14]S. Major, A. Banerjee, K. L. Chopra, and K. C. Nagpal, Thin Solid Films **143**, 19 (1986).
[15]H. Sato, T. Minami, and S. Takata, J. Vac. Sci. Technol. A **11**, 2975 (1993).
[16]A. Janotti and C. G. Van de Walle, Rep. Prog. Phys. **72**, 126501 (2009).
[17]M. D. Mccluskey and S. J. Jokela, J. App. Phys. **106**, 071101 (2009).
[18]A. Kobayashi, F. Sankey, and J. D. Dow, Phys. Rev. B **28**, 946 (1983).
[19]A. Tsukazaki, A. Ohtomo, T. Onuma, M. Ohtani, T. Makino, M. Sumiya, K. Ohtani, S. F. Chichibu, S. Fuke, Y. Segawa, H. Ohno, H. Koinuma, and M. Kawasaki, Nat. Mater. **4**, 42 (2004).
[20]E.-C. Lee, Y.-S. Kim, Y.-G. Jin, and K. Chang, Phys. Rev. B **93**, 235305 (2016).
[21]J. L. Lyons, A. Janotti, and C. G. Van de Walle, Appl. Phys. Lett. **95**, 252105 (2009).
[22]N. H. Nickel, F. Friedrich, J. F. Rommeluère, and P. Galtier, Appl. Phys. Lett. **87**, 211905 (2005).
[23]N. H. Nickel and M. A. Gluba, Phys. Rev. Lett. **103**, 145501 (2009).
[24]S. Limpijumnong, X. Li, S.-H. Wei, and S. B. Zhang, Appl. Phys. Lett. **86**, 211910 (2005).
[25]M. A. Gluba and N. H. Nickel, Phys. Rev. B **87**, 085204 (2013).
[26]J. J. Zhu, L. Vines, T. Aaltonen, and A. Y. Kuznetsov, Microelectron. J. **40**, 232 (2009).
[27]T. M. Børseth, F. Tuomisto, J. S. Christensen, E. V. Monakhov, B. G. Svensson, and A. Y. Kuznetsov, Phys. Rev. B **77**, 1 (2008).
[28]J. G. Reynolds, C. L. Reynolds, A. Mohanta, J. F. Muth, J. E. Rowe, H. O. Everitt, and D. E. Aspnes, Appl. Phys. Lett. **102**, 152114 (2013).
[29]D. C. Park, I. Sakaguchi, N. Ohashi, S. Hishita, and H. Haneda, Appl. Surf. Sci. **203–204**, 359 (2003).
[30]H. Zhang, W. Li, G. Qin, H. Ruan, D. Wang, J. Wang, Z. Huang, F. Wu, C. Kong, and L. Fang, Appl. Surf. Sci. **509**, 144793 (2020).
[31]K. Shi, P. F. Zhang, H. Y. Wei, C. M. Jiao, P. Jin, X. L. Liu, S. Y. Yang, Q. S. Zhu, and Z. G. Wang, J. Appl. Phys. **110**, 113509 (2011).
[32]M. H. Brodsky, M. A. Frisch, J. F. Ziegler, and W. A. Lanford, Appl. Phys. Lett. **30**, 561 (1977).
[33]N. H. Nickel, Phys. Rev. B **73**, 195204 (2006).
[34]N. H. Nickel and K. Brendel, Phys. Rev. B **68**, 193303 (2003).
[35]V. I. Anisimov, F. Aryasetiawan, and A. Lichtenstein, J. Phys.: Condens. Matter **9**, 767 (1997).
[36]A. Janotti and C. G. Van de Walle, Phys. Rev. B **74**, 045202 (2006).
[37]G. Henkelman, B. P. Uberuaga, and H. Jónsson, J. Chem. Phys. **113**, 9901 (2000).
[38]G. Kresse and J. Furthmüller, Phys. Rev. B **54**, 11169 (1996).
[39]G. Kresse and J. Joubert, Phys. Rev. B **59**, 1758 (1999).
[40]T. C. Damen, S. P. S. Porto, and B. Tell, Phys. Rev. **142**, 570 (1966).
[41]J. Crank, *The Mathematics of Diffusion*, 2nd ed. (Oxford University Press, 1975).
[42]W. B. Jackson and C. C. Tsai, Phys. Rev. B **45**, 6564 (1992).
[43]K. M. Johansen, L. Vines, T. S. Bjørheim, R. Schifano, and B. G. Svensson, Phys. Rev. Appl. **3**, 1 (2015).
[44]W. Beyer and H. Wagner, J. Appl. Phys. **53**, 8745 (1982).
[45]W. Beyer, in *Hydrogen in Semiconductors II*, edited by N. H. Nickel (Academic Press, San Diego, 1999), p. 165.
[46]W. B. Jackson, A. J. Franz, H.-C. Jin, J. R. Abelson, and J. L. Gland, J. Non-Cryst. Solids **227–230**, 143 (1998).
[47]C. Herring and N. M. Johnson, in *Hydrog. Semicond.*, edited by J. I. Pankove, and N. M. Johnson (Academic Press, San Diego, 1991), p. 225.
[48]N. H. Nickel, W. B. Jackson, and J. Walker, Phys. Rev. B **53**, 7750 (1996).
[49]See https://www.sigmaaldrich.com/certificates/COFA/20/ for "Sigma-Aldrich, ZnO Certif" (2021).
[50]L. N. Bai, J. S. Lian, W. T. Zheng, and Q. Jiang, Cent. Eur. J. Phys. **10**, 1144 (2012).
[51]N. S. Parmar and K. G. Lynn, Appl. Phys. Lett. **106**, 022101 (2015).
[52]P. Sharma, A. Gupta, K. V. Rao, F. J. Owens, R. Sharma, R. Ahuja, J. M. O. Guillen, B. Johansson, and G. A. Gehring, Nat. Mater. **2**, 673 (2003).
[53]T. Kataoka, M. Kobayashi, Y. Sakamoto, G. S. Song, A. Fujimori, F. H. Chang, H. J. Lin, D. J. Huang, C. T. Chen, T. Ohkochi, Y. Takeda, T. Okane, Y. Saitoh, H. Yamagami, A. Tanaka, S. K. Mandal, T. K. Nath, D. Karmakar, and I. Dasgupta, J. Appl. Phys. **107**, 033718 (2010).
[54]S. J. Jokela and M. D. McCluskey, Phys. Rev. B **76**, 6 (2007).
[55]P. Erhart, A. Klein, and K. Albe, Phys. Rev. B **72**, 085213 (2005).